January 2016

First proof of bismuth oxide nanoparticles as efficient radiosensitisers on highly radioresistant cancer cells

Callum Stewart
University of Wollongong, cl221@uowmail.edu.au

Konstantin K. Konstantinov
University of Wollongong, konstan@uow.edu.au

Sally McKinnon
University of Wollongong, srm286@uowmail.edu.au

Susanna Guatelli
University of Wollongong, susanna@uow.edu.au

Michael L. F Lerch
University of Wollongong, mlerch@uow.edu.au

See next page for additional authors

First proof of bismuth oxide nanoparticles as efficient radiosensitisers on highly radioresistant cancer cells

Abstract

This study provides the first proof of the novel application of bismuth oxide as a radiosensitiser. It was shown that on the highly radioresistant 9L gliosarcoma cell line, bismuth oxide nanoparticles sensitise to both kilovoltage (kVp) or megavoltage (MV) X-rays radiation. 9L cells were exposed to a concentration of 50 $\mu g.mL^{-1}$ of nanoparticle before irradiation at 125 kVp and 10 MV. Sensitisation enhancement ratios of 1.48 and 1.25 for 125 kVp and 10 MV were obtained *in vitro*, respectively. The radiation enhancement of the nanoparticles is postulated to be a combination of the high Z nature of the bismuth (Z = 83), and the surface chemistry. Monte Carlo simulations were performed to elucidate the physical interactions between the incident radiation and the nanoparticle. The results of this work show that Bi_2O_3 nanoparticles increase the radiosensitivity of 9L gliosarcoma tumour cells for both kVp and MV energies. Monte Carlo simulations demonstrate the advantage of a platelet morphology.

Keywords

first, oxide, proof, cancer, cells, nanoparticles, efficient, radiosensitisers, highly, bismuth, radioresistant

Disciplines

Medicine and Health Sciences

Publication Details

Stewart, C., Konstantinov, K., McKinnon, S., Guatelli, S., Lerch, M., Rosenfeld, A., Tehei, M. & Corde, S. (2016). First proof of bismuth oxide nanoparticles as efficient radiosensitisers on highly radioresistant cancer cells. Physica Medica: an international journal devoted to the applications of physics to medicine and biology, 32 (11), 1444-1452.

Authors

Callum Stewart, Konstantin K. Konstantinov, Sally McKinnon, Susanna Guatelli, Michael L. F Lerch, Anatoly B. Rosenfeld, Moeava Tehei, and Stephanie Corde

Graphical Abstract (for review)

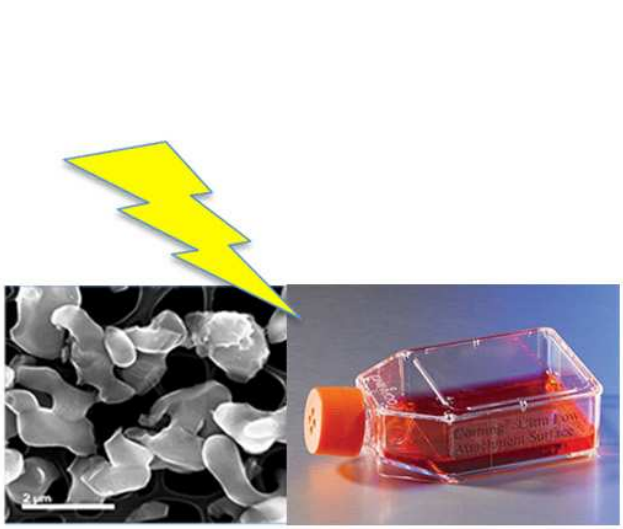

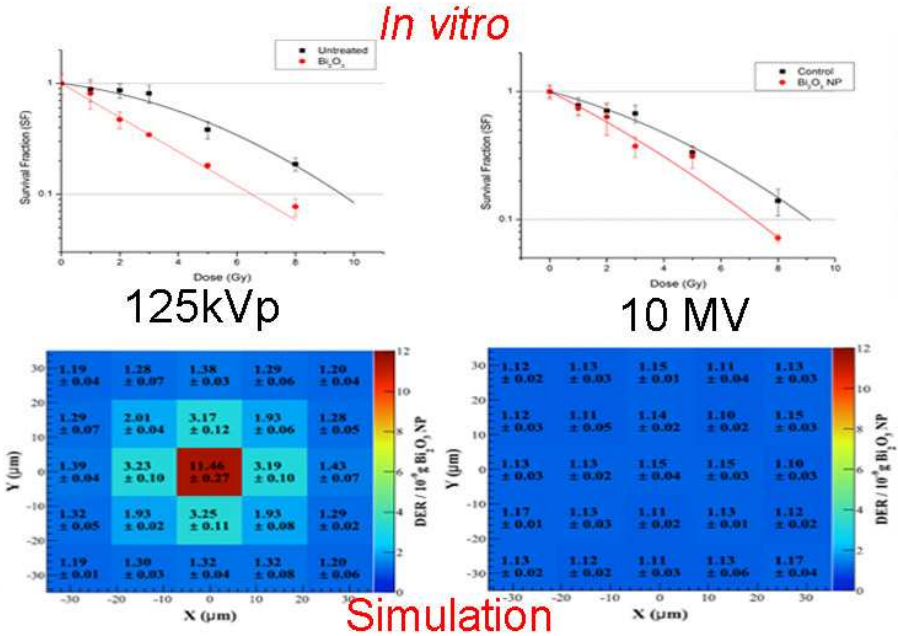

Physica Medica Highlights

- Bi_2O_3 nanoceramics are a prime candidate for radioenhancement cancer therapy
- First published surface area measurement of NPs at 48.7 ± 4.5 $cm^2.g^{-1}$
- SER of Bi_2O_3 shown to be 1.48 and 1.25 for 125kVp and 10MV *in vitro* on 9L
- Geant 4 Monte Carlo simulations predicted radiation dose enhancement in kilovolt but not megavolt

First proof of bismuth oxide nanoparticles as efficient radiosensitisers on highly radioresistant cancer cells

Callum Stewart[a,b,c],

Konstantin Konstantinov[b,c],

Sally McKinnon[d],

Susanna Guatelli[c,d],

Michael Lerch[c,d],

Anatoly Rosenfeld[c,d],

Moeava Tehei*[,c,d],

Stéphanie Corde[c,d,e].

[a] School of Chemistry, University of Wollongong, Northfields Ave, NSW, 2522, Australia
[b] Institute of Superconducting and Electronic Materials (ISEM), University of Wollongong, Squires Way, North Wollongong , NSW, 2500, Australia.
[c] Illawarra Health and Medical Research Institute (IHMRI), University of Wollongong, Northfields Ave, NSW, 2522, Australia.
[d] Centre of Medical and Radiation Physics (CMRP), University of Wollongong, Northfields Avenue, Wollongong, NSW, 2522, Australia.
[e] Radiation Oncology Department, Prince of Wales Hospital, Randwick, High Street, NSW, 2031, Australia

* corresponding author. Centre of Medical Radiation Physics (CMRP), University of Wollongong, Northfields Avenue, Wollongong, NSW, 2522, Australia.
email address: moeava@uow.edu.au (Moeava Tehei)

Abstract

This study provides the first proof of the novel application of bismuth oxide as a radiosensitiser. It was shown that on the highly radioresistant 9L gliosarcoma cell line, bismuth oxide nanoparticles sensitise to both kilovoltage (kVp) or megavoltage (MV) X-Rays radiation. 9L cells were exposed to a concentration of 50 $\mu g.mL^{-1}$ of nanoparticle before irradiation at 125kVp and 10MV. Sensitisation enhancement ratios of 1.48 and 1.25 for 125kVp and 10MV were obtained *in vitro*, respectively. The radiation enhancement of the nanoparticles is postulated to be a combination of the high Z nature of the bismuth (Z=83), and the surface chemistry. Monte Carlo simulations were performed to elucidate the physical interactions between the incident radiation and the nanoparticle. The results of this work show that Bi_2O_3 nanoparticles increase the radiosensitivity of 9L gliosarcoma tumour cells for both kVp and MV energies. Monte Carlo simulations demonstrate the advantage of a platelet morphology.

Key words: Bismuth oxide nanoparticles, radiosensitisers, Dose enhancement, Monte Carlo simulation.

1. Introduction

External X-ray Radiation Therapy is a common treatment for many cancers, which has been used extensively for many years. Despite the improvement of this cancer modality [1, 2], there are still unwanted side effects which need to be addressed [3].

One possible solution to improve the efficacy of X-ray radiotherapy exists in the use of metal nanoparticles (NPs) as individual radiosensitising agents. Investigations into gold NPs [4-7] and Platinum [8, 9] NPs were performed to quantify the biocompatibility of the proposed nanomaterials. The metallic NPs were shown to be radioenhancing under kilovolt (kVp) and megavolt (MV) radiation fields, however, they presented two problems. First, there was no guarantee that these nanomaterials would be biocompatible on the nanoscale. Studies into pure metal NPs showed that the size and morphology of the nanoparticle often resulted in varying degrees of toxicity [10, 11]. Metal NPs with diameters below 5 nm can freely diffuse into the nucleus and interact directly to DNA, resulting in necrosis [9, 10]. Second, the metals used for radiosensitisation require a high atomic number (high Z), and are also heavy metals. It was shown that these NPs induced toxicity as the treatment concentrations increased.

To solve these two issues, high Z nanoceramics, such as the promising tantalum pentoxide Ta_2O_5 [12], have started to be investigated. The Ta_2O_5 nanoparticle aggregates demonstrated the required radiosensitisation provided by the heavy Ta metal, and also the necessary biocompatibility thanks to the oxide form.

Bismuth is a better candidate for high Z radiosensitiser research since it is one of the heaviest naturally occurring elements of the periodic table [13]. Bismuth oxide and other bismuth-based compounds are also known to be biocompatible [14]. They have been extensively used in many medical and cosmetic applications for many years [15]. In addition, Stewart et al [16] showed that bismuth oxide nanoparticles could be tailored with different oxygen contents, inducing cell proliferation or toxicity. Another paper by Bogusz et al [17] highlighted that a theranostic system based on bismuth oxide nanoparticles would be highly effective in the treatment of cancer.

This research is aimed to investigate the novel application of high Z bismuth oxide nanoparticles as radiosensitisers for cancer therapy. The bismuth oxide nanoparticles were synthesised and irradiated with clinical 125 kVp and 10 MV X-ray beams. The cell clonogenic and internalisation assays were then performed. Monte Carlo simulations performed complemented the experimental work providing insight into the physical mechanisms behind dose enhancement and the effect of the particle morphology on these physical mechanisms.

2. Methods and Materials

2.1 Experimental

2.1.1 Synthesis

The bismuth based compounds were fabricated at the Institute of Superconducting and Electronic Materials (ISEM). The biocompatible Bi_2O_3 nanoparticles were synthesised via the precipitation route [16, 18]. Bismuth Nitrate (99.9 %, Sigma-Aldrich, Australia) was dissolved in 70% Nitric acid (50-70% Merck, Australia), and then 30% Ammonium Hydroxide (Sigma Aldrich, Australia) was added in small increments until a white precipitate appeared. This was extracted using a centrifuge and washed with deionised (DI) water. The precipitate was transferred to a beaker of DI water and stirred continuously for 5.5 hours at 100˚C. The precursor was extracted and washed as before then annealed under argon for 4 hours in a tube furnace at 530˚C.

2.1.2 X-ray diffraction (XRD)

The Bi_2O_3 was examined using an Enhanced Mini-Materials Analyser (EMMA) X-Ray Diffractometer at 40 kV and 25 mA. The X-ray diffractometer scanned between 20˚ and 80˚ at a step rate of 2.00˚min^{-1} and step size of 0.02˚. The mean crystalline size was determined using the Scherrer equation, while the material phase was extracted from the ICDD database using the Traces software [19, 20].

2.1.3 Surface area

The surface area of the nanoparticles was examined using the methylene blue test due to negative effects induced by the drying process of Brunauer Emmet Teller (BET) gas adsorption surface area method. Bismuth oxide (100 mg) was dispersed in 50 mL deionised (DI) water and 12 mg of Methylene Blue (MB) added. After stirring and leaving overnight, a sample was taken from the stock and diluted accordingly for UV-vis analysis. The absorption at 665 nm of the MB solution was measured using a Shimatzu 3600 NIR UV-vis Spectrophotometer (Shimadzu, Kyoto, Japan). After examination, 4 mg of MB was added to the stock with 5 mL of DI. This was repeated for three days until the ideal concentration was determined. The concentrations were converted to weight ratios of the adsorbed MB: Bi_2O_3 and the added MB: Bi_2O_3. The ratio values were plotted against each other to produce the Langmuir curve and the ion replacement concentration point was used to determine the specific surface area (SSA) according to the following equation [21]:

$$SSA = \frac{m_{MB}}{319.87} . A_V . A_{MB} . \frac{1}{m_s} \quad (1)$$

where m_{MB} is the weight of MB added, 319.87 $g.mol^{-1}$ is the MB molecular weight, A_V is Avogadro's number ($6.023*10^{23}$ mol^{-1}), A_{MB} is the accepted surface area of a single adsorbed MB molecule ($130Å^2$) [21] and m_s is the weight of the Bismuth oxide.

2.1.4 Cell internalisation

Cell internalisation was performed at at the Illawarra Health and Medical Research Institute (IHMRI). A LSRII (BD, Franklin Lakes, NJ, USA) Fluorescence Activated Cell Sorting (FACS) flow cytometer was used in order to determine the degree of internalisation of the nanomaterials into the cultured 9L cells. This was done as part of an oxidative stress assay [16]. The cells were brought to 90% confluence in T12.5cm^2 flasks (Falcon®, Corning). Twenty four hours before the procedure, $2x10^4$ cells were transferred to 5 mL flow cytometer tubes and freshly prepared NP solution was added to the designated NP sample tubes, filling to 0.5 mL total volume at 50 $\mu g.mL^{-1}$. After 24 hours the tubes were agitated to dislodge the cells and were analysed with a flow rate of 60 $mL.min^{-1}$ until

10 000 events were recorded. The degree of internalisation of the nanomaterials was determined with FACSDiva software, assessing both forward and side scatter intensities [17, 22].

2.1.5 Media preparation

The 9L gliosarcoma cells were maintained in a T75cm^2 flask with completed Dulbecco's Modified Eagle Medium (c-DMEM) (DMEM from GIBCO, supplemented with 10% Fetal Bovine Serum (FBS) and 1% Penicillin and Streptomycin) and incubated at 37 ˚C with 5% (v/v) CO_2 [12].

2.1.6 Determination of Bi_2O_3 k-edge and optimum kVp radiation

To optimise the dose enhancement effects of the bismuth oxide the correct filter and beam energy needed to be calculated. This optimal energy was the closest to the maximum photon mass absorption energy for the bismuth oxide compared to water, maximising the secondary photoelectric particle production. Using the Xmudatv1.0.1 program the photo attenuation coefficients for water and bismuth oxide were generated based on total mass energy absorption. The ratio between the two curves was graphed as a function of energy [12].

2.1.7 Irradiation with kVp and MV beams

All irradiation experiments were carried out at the radiation oncology department of the Prince of Wales Hospital (Randwick, NSW, Australia). Beam energies of 125 kVp and 10 MV were generated by a Nucletron Oldelft Therapax DXT 300 Series 3 Orthovoltage unit (Nucletron B.V., Veenendaal, The Netherlands) and an Elekta Axesse^{TM} LINAC (Elekta AB, Kungstensgatan, Stockholm, Sweden), respectively.

Cell culturing and clonogenic assays were performed at IHMRI. The 9L cell culture was brought to 90% confluence a day prior to irradiation. 50 µg.mL^{-1} of Bismuth oxide NPs was prepared via sonication with a double step Branson 250 Digital sonifier at 70% amplitude for 3x 10 minutes runs.

The suspension was added to the cell culture medium of the treated samples for 24 hours while the untreated controls were not. For kVp experiments, 9L cells were irradiated in T12.5 cm^2 flasks (BD Falcon ^{TM}) with 6 mm of medium. For MV experiments, T12.5 cm^2 flasks were completely filled with Hank's Balanced Salt Solution (HBSS). No air bubbles were present inside the flask to ensure that electronic equilibrium was obtained at cell monolayer depth. All doses (1, 2, 3, 5, & 8 Gy) were delivered in single fractions at room temperature. Tissue culture flasks were laid horizontally and surrounded sides and back by a 30x30x10 cm^3 solid water phantom to ensure backscattering effects were taken into account. The flasks were then irradiated with the source perpendicular (z-axis) to the flasks. Irradiated flasks of the same dosage were irradiated together to reduce individual dose variation. Non-irradiated control samples, with and without bismuth oxide NPs, were handled under the same conditions as the irradiated samples [12]. The experiments were performed in triplicate with multiple repetitions.

2.1.8 Clonogenic cell survival assay

Clonogenic assay was used as the radiobiological endpoint to assess the effects of 50 $\mu g.mL^{-1}$ concentration of bismuth oxide NPs on cell survival, compared to control (no NPs). After irradiation, cells were sub-cultured at low density into 100 mm diameter Petri dishes (Sigma) with 10 mL c-DMEM and incubated for 15 doubling times. Following this, each dish was washed with 5 mL PBS (with calcium and magnesium ions) and fixed and stained with 5 mL of a (25% crystal violet, 75% ethanol) solution. Colonies consisting of no less than 50 cells were counted (n) and compared with initial seeding values (I) to obtain the plating efficiency (PE) [12, 16], expressed as:

$$PE = n/I \qquad (2)$$

For each group, the surviving fraction (SF) is determined as the ratio of the PE of the irradiated sample (PE_x) by PE of the non-irradiated control (PE_c):

$$SF = PE_x / PE_c \qquad (3)$$

2.1.9 *Cell survival analysis*

Survival curves were fit according to the linear quadratic model (LQM) using the associated error bars of each point as weighting factors. The LQM describes cell surviving fraction (SF) mathematically as a function of absorbed dose (D). The fit parameters, α (Gy^{-1}) and β (Gy^{-2}), are indicative of cell radiosensitivity and repair effectiveness, respectively [7]. They are derived from the LQM equation (4):

$$SF(D) = \exp(-\alpha D - \beta D^2) \quad (4)$$

We quantified the degree of dose enhancement introduced by the NPs by means of the Sensitisation Enhancement Ratio (SER), defined as the ratio of doses giving 10% cell surviving fraction. SER represents a radioenhancement based on the radiobiological endpoint from the LQM curves, and is dependent upon the delivered dose [5].

2.2 *Monte Carlo Simulation*

Simulations were performed using Geant4 (version 9.6 patch 2), a Monte Carlo code modelling particle transport through matter [23], at the Centre for Medical and Radiation Physics (CMRP). The simulation set-up was modelled to retain the essential characteristics of the experimental configuration necessary to investigate the physical mechanisms behind the results of the cell experiments and to investigate the effect of the shape of the NP aggregate on the energy deposition enhancement.

The geometry consisted of a cell population modelled as an array of spherical water cell volumes with 10 μm diameter (shown in Figure 1), placed in a water phantom at a depth of 6 mm and 25 mm for kVp and MV beams, respectively, to obtain electronic equilibrium. The dimensions of the phantom reflect the sizes of the real phantom used in the experiments. Geant4 Low Energy electromagnetic physics was used with Penelope models to describe the interactions of particles down to 100 eV in the cell population. Atomic deexcitation processes (including both fluorescence and Auger electron emission) were activated in the simulation.

The NP aggregate was modelled as a sphere of 10 μm diameter, a cube with 10 μm sides or a plate with dimensions 10 μm x 10 μm x 1 μm, placed at the centre of the cell populations, as shown in Figure 1.

The energy spectra of 125 kVp and 10 MV X-ray beams were simulated using SpekCalc v 1.1 [24] and provided by ARPANSA [25], respectively. A 100 μm x 100 μm beam of photons was incident normally on the phantom edge, along the Z axis (see Figure 2). A total of 6 x 10^6 and 3.5 x 10^6 primary photons were incident on the phantom in order to achieve sufficient statistical results in the kVp and MV beam simulations, respectively.

The energy deposited in each cell was calculated with and without the NP. In this study, the dose enhancement factor (DEF) was defined as a ratio D_{NP}/D_C*, where D_{NP} and D_C* are the doses calculated with and without the Bi_2O_3 NP aggregate placed in the cell array, as shown in Figure 1. Water substituted Bi_2O_3 in the simulation configuration without the NP. The DEF represents the physical dose enhancement due to the interactions of incident photon beam and the NP, and is independent of delivered dose.

The DEF was calculated for the different shapes of the NP nanomaterial under study. This factor depends on the mass and shape of the NP aggregate. In order to isolate the effect of the increasing mass of the NP aggregates, the DEF was scaled with respect to the NP aggregate mass. The scaled DEF, referred to as DEF_S, was calculated as DEF/m_{NP} where m_{NP} is the mass of the NP aggregate placed in the cell population. In order to evaluate the effect of the NP aggregate shape (in terms of increasing surface area to volume ratio), the DEF and DEF_S were compared.

The spectra and the Linear Energy Transfer (LET) of secondary electrons produced by the incident X-ray beam were calculated.

3. Results

3.1 Experimentation

3.1.1 X-ray Diffraction

The bismuth oxide nanoparticles were characterised as alpha phase [26] by the XRD spectrum. The Scherrer equation was applied to the three peaks (1 2 0), (2 0 0), and (-2 2 1) which showed the Bi_2O_3 nanoparticles had a size range of range of 50 – 70nm. This can be observed in Figure 3, denoted by the transparency of the platelets.

3.1.2 Surface area

The optimal MB concentration for the 100 mg of bismuth oxide nanoparticles was determined to be 0.26 ± 0.02 $mg.mL^{-1}$. Using the cation replacement point, the surface area of the NPs was determined to be 48.7 ± 4.5 $cm^2.g^{-1}$. There is currently no literature value for comparison. Correct sonication played a crucial role in this process due to the tendency of the nanoparticles to aggregate.

3.1.3 Cell internalisation

The comparison of side scatter (SSC) v.s. forward scatter (FSC) light values at 24 hours showed a dramatic increase in the side scatter of the NPs samples over the control. The SSC is proportional to the cell granularity and can be used to examine the cellular uptake of the nanoparticles [27]. The relative increase in scatter is 7 times higher than the controls indicating that a large quantity of nanoparticles had been taken into the cells, as denoted by the dramatic change in scatter distribution (Figure 4).

3.1.4 kVp energy determination

The maximum differential absorption energy is around 40 keV with the K-edge being located at 91 keV (Figure 5). These values were then examined against the available spectra for the kVp orthovoltage unit at Prince of Wales Hospital and it was determined that filter 4 would be the most suitable. Filter 4 is an additional filtration of 0.1 mm Cu and 0.25 mm Al; in combination with an X-ray tube potential of 125 kVp orthovoltage beam, it produces photons with an effective energy of 46.7 keV (Figure 2).

3.1.5 *Intrinsic toxicity, survival curves, and radiosensitivity parameters*

The Bi_2O_3 NP used in this experiment underwent argon annealing and were found to have no cytotoxicity on 9L cells as previously described [16]. The first radiation energy examined was 125 kVp, which corresponds to the calculated optimum energy of Bi_2O_3 (see Figure 5), and is used for treatment of superficial cancers. The extracted α and β parameters from the linear quadratic curves were 0.075 ± 0.040 Gy^{-1} and 0.017 ± 0.006 Gy^{-2} for the control sample and 0.355 ± 0.003 Gy^{-1} and 0 Gy^{-2} for the cells with Bi_2O_3. This lead to an SER of 1.48 for the Bi_2O_3 NP at 125 kVp, demonstrating that the material is a highly effective radiosensitiser (Figure 6).

The effect of bismuth oxide nanoparticles was also examined with 10 MV radiation to investigate how effective it would be for treating deeper seeded cancers, like brain cancer (Figure 7). The extracted α and β parameters from the linear quadratic curves were 0.150 ± 0.030 Gy^{-1} and 0.013 ± 0.005 Gy^{-2} for the control sample and 0.256 ± 0.054 Gy^{-1} and 0.009 ± 0.007 Gy^{-2} for the cells with Bi_2O_3. The analysis of the curves produced an SER of 1.25 for the Bi_2O_3 nanoparticles.

3.2 *Results of the simulation study*

3.2.1 *Effect of NP aggregate geometry in dose enhancement*

The physical dose enhancement produced by the Bi_2O_3 sphere, cube, and plate placed in the cell population was calculated in terms of DEF and DEF_S as explained in the Methodology section. Figure 8 shows the DEF and DEF_S in cells with respect to radial distance from NP centre in cell layer 3, downstream of the NP, and cell layer 2, containing the NP, in the 125 kVp X-ray field.

Table 1 shows the total DEF and DEF_S obtained when considering the three alternative Bi_2O_3 NP aggregate geometries. It can be observed that the DEF obtained in the case of a cube is larger than that of the sphere and plate configurations, however, when the DEF_S is considered, the plate geometry is superior in terms of dose enhancement. This is due to the higher surface area to volume ratio in the case of the plate (2.4×10^6), compared to the surface area to volume ratios of the cube and sphere

(both equal to 0.6 x 10^6). Since the in vitro conditions assume a monolayer of cells at the time of irradiation, the cells in the bottom layer (layer 3 in Figure 1) below the NP aggregate are also shown in Table 1.

3.2.2 Secondary electron spectra

The kinetic energy and LET spectra of secondary electrons entering all the cells in the population were analysed to assess the change in the quality of the secondary electrons due to the presence of each NP aggregate shape. The results are shown for the kVp and MV beam in Figure 9 where the spectra are shown per incident photon on the water phantom. It can be observed that the secondary electron spectra and LET are not significantly enhanced by the Bi_2O_3 NP in the 10 MV photon field. This is in contrast to the kilovoltage case where there is a clear enhancement of the secondary electron production. In particular, the greatest increase in number of secondary electrons is observed in the case of the cube geometry, followed by the sphere and plate.

These secondary electron spectra results agree with the DEF reported in Table 1 for the 125 kVp and 10 MV photon fields, respectively. The enhancement of secondary electron production is dependent on the geometry with the cube geometry providing the highest number of secondary electrons due to the absolute increase in the mass of Bi_2O_3 NP material placed in the cell population.

When the DEF_s is calculated, it is observed that the plate geometry is the most efficient enhancer. This is due to the increased chance of secondary electrons to be absorbed within the NP aggregate itself with increasing geometrical size and lower surface area to volume ratio. The plate geometry allows more electrons to escape the surface, as the thickness of the plate is only 1 μm, and the range of which is less than the range in Bi_2O_3 of a 12 keV electron [28], meaning most of the electrons will be able to escape the NP geometry. By contrast, the range of a 50 keV electron in Bi_2O_3 is 10.6 μm which means that electrons originate in the cube with energy lower than this value will have a reduced probability of escaping.

4. Discussion

The MB surface area method provided two advantages over the BET. The first was that the suspension was a closer match for the liquid cell environment, closer simulating the actual particle size found during testing. The second was that in suspension, the full surface area could be measured as the nanoplatelets aggregate when dried and lose access to the majority of their surface area.

Cell internalisation measurement showed that the nanoparticles were highly internalised after 24 hours (Figure 4). However, due to the physical parameters of the nanoparticles, the Bi_2O_3 NPs should not penetrate the nucleus and interfere with the DNA resulting in NP induced apoptosis, as is the case of nanoparticles with diameters smaller than 5 nm [10].

Both Geant4 simulations and *in vitro* experiments were essential for this study. The simulations provided insight into the physical processes behind physical dose enhancement in the cells, whereas *in vitro* measurements allowed the study of the synergy among physical, chemical, and biological mechanisms when enhancing radiotherapy treatment by means of nanoparticles.

The Geant4 simulations demonstrated that in the kVp X-ray field, Bi_2O_3 had considerable physical dose enhancement properties, with a dependence on the NP aggregate geometrical shape, related to Surface Area to Volume ratio (SA/V). The dose enhancement was shown to be significant (DEF around 2-3 in the cell population studied, depending on the geometry of the nanoparticle aggregate) in the 125 kVp photon field compared to no significant dose enhancement calculated in the 10 MV field. This is due to the strong increase in photoelectric effect cross-section in the kVp energy range for high Z materials, whereas, electron pair production dominates at 10 MV with contributions from Compton scattering. This effect is caused by the strong Z-dependence (approximately power 3-4) of the photoelectric effect compared to pair production (above 1.022 MeV), which has mass attenuation coefficient approximately proportional to Z, and Compton scattering, which is not strongly Z-dependent [29]. This means that the higher energy photons in the 10 MV spectra are unlikely to strongly contribute to radiation dose enhancement. The megavoltage simulation study found no significant enhancement for any NP morphologies studied. The simulation results for Bi_2O_3 under a kilovoltage beam are in agreement with the experimental data published by Alqathami et al [30].

The cell survival curves (Figures 6 and 7) showed that the bismuth oxide has an SER of 1.48 and 1.25 in kVp and MV beam, respectively. The highest SER values for Au NPs is an enhancement of 1.41 obtained at 150 kVp on a less radioresistant cell line. The SER reduced when the Au NPs were examined in more resistant cells [5]. Tantalum oxide has shown an SER of 1.33 on 9L cells at 10MV [12]. The DEF observed in the simulated cell population was 1.87 ± 0.01 in the layer of cells below the Bi_2O_3 NP plate in the 125 kVp X-ray field. This is a DEF calculated in a small number of cells close to the NP aggregate in this simulation and cannot be compared directly to the experimental SERs observed. However, the High-Z dose enhancement properties of Bi_2O_3 NPs are an important factor influencing increased SER and the calculated DEF from the Monte Carlo simulation reflects this.

The effectiveness of any nanoparticle system in radiation fields is due to a number of factors including cell line, radiation energy, particle morphology, subcellular localisation, and concentration. The 9L gliosarcoma cells used in this study are known to be more radio-resistant and more hypoxic than most of other cancerous cells. Oxygen levels in cells have been shown to alter the effectiveness of radiation therapy, as oxygen is responsible for indirect damage through radiation induced radicals [31]. Therefore, observations on 9L cells should be amplified on less radio-resistant and hypoxic cells.

The surface chemistry of the nanoparticles also has an important effect on the effectiveness of the radiosensitiser as indirect damage is the major mechanism behind cancer apoptosis in radiation therapy [32]. It has been shown that nanoparticles can demonstrate catalytic behavior under radiation fields becoming radiocatalysts. In the case of our NPs, it is hypothesized that the energy of the photons excite the NPs, causing them to act as radiocatalysts and split water molecules into $HO^{\cdot}$ and $H^{\cdot}$ radicals [33]. This produces additional ROS which increases the effectiveness of the radiosensitiser and would not be predicted in simulations.

The morphology (SA/V) of the radiosensitising NPs also plays an important role in their effectiveness. The Monte Carlo simulations were designed to model the experimental set up, as stated in section 2.2, with the incident x-ray beam along the Z-axis. Each 10μm diameter cell within the array was measured and the average DEF taken for the entire population. Comparatively, the

internalisation assay demonstrated high levels of NP internalisation 24 hours after NP exposure within the biological cell monolayer (section 3.1.3.), with the incident x-ray beam passing along the z-axis, perpendicular to the cell monolayer (section 2.1.7). The Monte Carlo simulations demonstrated that the platelet morphology of Bi_2O_3 NP aggregates leads to more effective radiation damage, especially in kVp photon field, due to a larger SA/V ratio compared to the other morphologies as demonstrated by our Monte Carlo simulations in section 3.2. Therefore, according to the local effect model the platelet morphology leads to a more preferential dose spike distribution in the individual cellular environments for the same weighted concentration of NPs.

The apparent disparity between the Monte Carlo simulations and the *in vitro* survival curves can be explained through a comparison of the analysis techniques [34]. DEF calculations are the physical ratio of energy deposited with a NP aggregate compared to a pure water phantom. This produces DEF values which are independent of therapeutic dose for a given X-ray energy, i.e. 125 kVp or 10 MV. Alternatively, the SER is a radiobiological endpoint based on a quadratic exponential equation (eqn 4), with the radioenhancement being dependent upon the dose for a given X-ray energy, as seen in Figures 6 and 7, and does not scale linearly.

The Local Effect Model (LEM) for radiation enhancement assists in describing the NP-radiation interactions in the biological context. It states that the dose enhancement of a single particle is effective only to a small subvolume of the total, i.e. the cytoplasm of a cell with an internalised NP. As shown in the Monte Carlo simulations, 50 keV electron has a range of up to 10.6 µm, meaning the subvolume affected by the NP under radiation is confined to the inside of a cell, given the average diameter of a eukaryotic cell is approximately 20-50 µm. Each subvolume produces a slight variation in the dose determined by the NP's interaction with the incident radiation field (dose spike distribution) [32]. While the amplitude and shape of the local dose spikes is different in the kVp and MV photon fields due to the LET of the radiation fields [35], both lead to a large SER. The physical dose enhancement is the cumulative effect of these NP-radiation field interactions, and produce the observed SER in combination with the previously mentioned radiocatalytic and SA/V factors.

5. Conclusion:

This work provided the first *in vitro* study of the radiosensitising capacity of bismuth oxide nanoparticles on the highly radioresistant 9L gliosarcoma cells. The XRD and MB analysis showed that the nanoparticles have a platelet morphology with a thickness of 50 – 70nm and a surface area of 48.7 ± 4.5 $cm^2.g^{-1}$. The Bi_2O_3 NP were irradiated with 125 kVp and 10 MV x-ray beams, producing SERs of 1.48 and 1.25 respectively. These values are resultant from a combination of the high Z of the bismuth, radiocatalytic activity, and the favourable dose distribution resulting from the advantageous geometrical shape of the nanoparticles on the highly radioresistance 9L cells.

Monte Carlo simulations are a valuable tool to examine the physical dose enhancement of NP enhanced radiotherapy and the importance of careful simulation design to accurately model NP geometry has been demonstrated. Simulations showed that the platelet morphology per unit of Bi_2O_3 mass, is the most effective for enhancing the dose, compared to the cubic and spherical morphologies. The DEF reported by the simulation study are lower than the biological SER found by means of the cell survival experiments in both the kVp and MV radiation fields due to the non-linear dose enhancement nature of biological systems. The means that the physical dose enhancement induced by the High-Z of Bi_2O_3 is only one of multiple factors influencing the sensitisation and this is the only factor accounted for in the simulated DEF in the cell population compared to the experimental SER measurements.

Acknowledgements:

Funding: This work was supported by the National Health and Medical Research Council (NHMRC) Grant [APP1084994]

References:

1. Connell, P., and Hellman, S. **Advances in radiotherapy and implications for the next century: A historical perspective.** *Cancer Res.*, 2009, 69(2), pp.383-392
2. Baskar, R., Lee, K., Yeo, R., and Yeoh, K. **Cancer and radiation therapy: current advances and future directions.** *Int. J. Med. Sci.*, 2012, 9(3), pp.193-199.

3. Bentzen, S. **Preventing or reducing late side effects of radiation therapy: radiobiology meets molecular pathology.** *Nat. Rev. Cancer.*, 2006, 6(9), pp.702-713.
4. Cifter,G., Chin, J., Cifter, F., Altundal, Y., Sinha, N., Sajo, E., et al. **Targeted radiotherapy enhancement during electronic brachytherapy of accelerated partial breast irradiation (APBI) using controlled release of gold nanoparticles.** *Phys Med*, 2015, 31(8), pp. 1070-1074.
5. Jain, S., Coulter, J., Hounsell, A., Butterworth, K., McMahon, S., Hyland, W., et al. **Cell-specific radiosensitisation by gold nanoparticles at megavoltage radiation energies.** *Int. J. Radiat. Oncol.*, 2011, 79(2), pp.531-539.
6. Rahman, W., Geso, M., Corde, S., Yagi, N., Aziz, S., and Annabell, N. **Optimal energy for cell radiosensitivity enhancement by gold nanoparticles using synchrotron-based monoenergetic photon beams.** *Int. J. Nanomed.*, 2014, 9, pp.2459–2467.
7. Butterworth, K. T., Coulter, J., Jain, S., Forker, J., Mcmahon, S., Schettino, G., et al. **Evaluation of cytotoxicity and radiation enhancement using 1.9 nm gold particles: potential application for cancer therapy.** *Nanotechnology*, 2010, 21 (29), 295101, pp. 1- 9.
8. Asharani, P., Xinyi, N., Hande, M., and Valiyaveettil, S. **DNA damage and p53-mediated growth arrest in human cells treated with platinum nanoparticles.** *Nanomedicine*, 2010, 5(1), pp.51-64.
9. Porcel, E., Liehn, S., Remita, H., Usami, N., Kobayashi, K., Furusawa, Y., et al. **Platinum nanoparticles: a promising material for future cancer therapy?** *Nanotechnology*, 2010, 21(8), 085103, pp.1-7.
10. Pan, Y., Neuss, S., Leifert, A., Fischler, M., Wen, F., Simon, U., et al. **Size-dependent cytotoxicity of gold nanoparticles**. *Small*, 2007, 3(11), pp.1941-1949.
11. Sun, Y.N., Wang, C.D., Zhang, X.M., Ren, L., and Tian, X.H. **Shape dependence of gold nanoparticles on in vivo acute toxicological effects and biodistribution.** *J Nanosci Nanotech.*, 2011, 11(2), pp.1210–1216.
12. Brown, R., Tehei, M., Oktaria, S., Briggs, A., Stewart, C., Konstantinov, K., et al**. High-Z nanostructured ceramics in radiotherapy: First evidence of Ta_2O_5 -induced dose enhancement on radioresistant cancer cells in an MV photon field**. *Part. Part. Syst. Charact.*, 2013, 31(4), pp.500-505.
13. Hossain, M., and Su, M. **Nanoparticle Location and Material-Dependent Dose Enhancement in X-ray Radiation Therapy.** *J. Phys. Chem. C*, 2012, 116(43), pp.23047-23052.
14. Levason W., and Reid G. in: **Comprehensive Coordination Chemistry II**, Meyer T. J., Ed. (Pergamon, Oxford, 2003), pp. 465-544.
15. Kim, E., Lee, B., Chang, H., Lee, W., Hong, C., et al. **Evaluation of the radiopacity and cytotoxicity of Portland cements containing bismuth oxide.** *Oral Surg. Oral Med. Oral Pathol. Oral Radiol Endod.*, 2008, 105(1), pp.54-57.
16. Stewart, C., Konstantinov, K., McDonald, M., Bogusz, K., Cardillo, D., Oktaria, S., et al. **Engineering of bismuth oxide nanoparticles to induce differential biochemical activity in malignant and nonmalignant cells.** *Part. Part. Syst. Charact.*, 2014, 31(9), pp.960-964.
17. Bogusz, K., Tehei, M., Stewart, C., McDonald, M., Cardillo, D., Lerch, M., et al. **Synthesis of potential theranostic system consisting of methotrexate-immobilized (3-aminopropyl) trimethoxysilane coated α-Bi_2O_3 nanoparticles for cancer treatment.** *RSC Adv*, 2014, 4(46), pp.24412-24419.
18. Patil, M., Deshpande, V., Dhage, S., and Ravi, V. **Synthesis of bismuth oxide nanoparticles at 100 ˚C**. *Mat. Lett.*, 2005, 59(19-20), pp.2523-2525.
19. Cardillo, D., Tehei, M., Lerch, M., Corde, S., Rosenfeld, A., et al. **Highly porous hematite nanorods prepared via direct spray precipitation method.** *Mat. Lett.*, 2014, 117, pp.279-282.
20. Warren, B. (1969), **X-ray Diffraction** (Addison-Wesley Series in Metallurgy and Materials). (Addison-Wesley, 1969), pp. 382
21. Santamarina, J.C, Klein, K.A., Wang, Y.H., and Prencke, E. **Specific surface: determination and relevance**. *Can Geotech J.*, 2002, 39(1), pp.233-241.

22. Böhme, S., Stärk, H.-J, Meißner, T., Springer, A., Reemtsma, T., Kühnel, D. et al. **Quantification of Al2O3 nanoparticles in human cell lines applying inductively coupled plasma mass spectrometry (neb-ICP-MS, LA-ICP-MS) and flow cytometry-based methods.** *J Nanopart Res.*, 2014, 16(9), 1-15
23. Allison, J., Amakoc, K., Apostolakis, J., Arce, P., Asai, M., Aso, T., *et al*. **Recent Developments in Geant4**, *Nucl. Instr. Meth. Phys. Res.A*, 2016, http://dx.doi.org/10.1016/j.nima.2016.06.125
24. Poludniowski, G., Landry, G., DeBlois, F., Evans, P., and Verhaegen, F. **SpekCalc: a program to calculate photon spectra from tungsten anode x-ray tubes.** *Phys Med Biol*, 2009, 54(19), pp.N433-N438.
25. Lye, J. E., Butler, D. J., Ramanathan G., and Franich R. D. **Spectral differences in 6MV beams with matched PDDs and the effect on chamber response.** *Phys. Med. Biol.*, 2012, 57(22): 7599-7614..
26. La, J., Huang, Y., Luo, G., Lai, J., Liu, C., and Chu, G. **Synthesis of bismuth oxide nanoparticles by solution combustion method.** *Particul Sci Tech*, 2013, 31(3), pp.287-290.
27. Suzuki, H., Toyooka, T., and Ibuki, Y. **Simple and easy methods to evaluate uptake potential of nanoparticles in mammalian cells using a flow cytometric light scatter analysis.** *Environ Sci Tech.*, 2007, 41(8), pp.3018-3024.
28. Berger, M. J., Coursey, J. S., Zucker, M. A., and Chang, J. **ESTAR, PSTAR, and ASTAR: Computer Programs for Calculating Stopping-Power and Range Tables for Electrons, Protons, and Helium Ions (version 1.2.3)**. 2005. Retrieved 04/04/2014, from http://physics.nist.gov/Star.
29. Attix, F. **Introduction to radiological physics and radiation dosimetry**. New York: Wiley. 1986.
30. Alqathami, M., Blencowe, A., Yeo, U., Franich, R., Doran, S., Qiao, G., et al. **Enhancement of radiation effects by bismuth oxide nanoparticles for kilovoltage x-ray beams: A dosimetric study using a novel multi-compartment 3D radiochromic dosimeter.** *J Phys Conf Ser*, 2013, 444, p.012025. doi:10.1088/1742-6596/444/1/012025.
31 Brown, J., and Wilson, W. **Exploiting tumour hypoxia in cancer treatment.** *Nat. Rev. Cancer*, 2004, 4(6), pp.437-447.
32. Kelada, O. **Advantages and disadvantages of charged particle therapy - Particle Therapy Cancer Research Institute**. [online] Ptcri.ox.ac.uk. 2014. Available at: http://www.ptcri.ox.ac.uk/about/literaturereview.shtml
33. Geng, F., Song, K., Xing, J., Yuan, C., Yan, S., Yang, et al. **Thio-glucose bound gold nanoparticles enhance radio-cytotoxic targeting of ovarian cancer.** *Nanotechnology*, 2011, 22(28), p.285101.
34. Ballarini, F. **From DNA Radiation Damage to Cell Death: Theoretical Approaches.** *J. Nucleic Acids*, 2010, pp.1-8.
35. Friedrich, T., Grün, R., Scholz, U., Elsässer, T., Durante, M., and Scholz, M. **Sensitivity analysis of the relative biological effectiveness predicted by the local effect model**. *Phys. Med. Biol.*, 2013, 58(19), pp.6827-6849.

Figure legends:

Figure 1: Cross-section in y-z plane of cell population with the NP modelled as a sphere (A), cube (B) or a plate (C) with the photon beam incident on the cell layer from the left along the Z axis. D: Cross-section in x-y plane through layer 2 of cells arrayed around 10 μm diameter sphere of Bi_2O_3.

Figure 2: 150 kVp (A) and 10MV (B) photon energy spectra, provided in terms of relative frequency per incident photon [26].

Figure 3: High resolution – transmission electron microscopy (HR-TEM) image of Bi_2O_3 nanoparticles platelets.

Figure 4: Nanoceramic internalisation, Side scatter (SSC) of 9L cells without (A) and with (B) nanoceramic

Figure 5: Ratio of mass energy absorption coefficient of Bi_2O_3 relative to water

Figure 6: Survival curves of 9L untreated and treated with 50 μg/ml of Bi_2O_3 nanoparticles and exposed to 125kVp x-ray radiation doses. Surviving fractions were normalised against the non-irradiated controls, averages taken from a sample size of 3 and errors given ± 1 standard deviation from the mean.

Figure 7: Survival curves of 9L cells untreated and treated with 50 μg/ml of Bi_2O_3 nanoparticles and exposed to 10 MV x-ray radiation doses. Surviving fractions were normalised against the non-irradiated controls, averages taken from a sample size of 3 and errors given ± 1 standard deviation from the mean.

Figure 8: Radial DER (A & C) and DER_S (B & D) in layer 3 (A & B) and layer 2 (C & D) in 125 kVp photon radiation field with Bi_2O_3 NP material in different geometrical configurations (Sphere, Cube, Platelet).

Figure 9: Kinetic energy and LET spectra of secondary electrons entering cells in the array with 125 kVp photon field, (A) and (B), and 10MV photon field, (C) and (D). Bi_2O_3 sphere (grey circles) compared to cube (black circles), plate (crosses) and water (hollow circle).

Table 1: DER and DER_S due to each NP aggregate configuration with 125 kVp and 10 MV incident photon fields. DER is calculated for the entire cell population and for the cells in layer 3 of the cell population (below the NP aggregate) to represent the monolayer of cells seen in cell survival experiments.

Table 1

		125 kVp		
		Sphere	Cube	Plate
Total cell population	DER	2.18 ± 0.01	3.27 ± 0.02	1.48 ± 0.01
	DER_S (g_{NP}^{-1})	(4.67 ± 0.02) x10^8	(3.68 ± 0.02) x10^8	(16.58 ± 0.07) x10^8
Cells in layer 3	DER	2.09 ± 0.02	3.06 ± 0.02	1.87 ± 0.01
	DER_S (g_{NP}^{-1})	(4.48 ± 0.03) x10^8	(3.44 ± 0.03) x10^8	(21.1 ± 0.2) x10^8
		10MV		
Total cell population	DER	1.005 ± 0.004	1.020 ± 0.007	1.002 ± 0.005
	DER_S (g_{NP}^{-1})	(2.16 ± 0.01) x10^8	(1.15 ± 0.01) x10^8	(11.26 ± 0.05) x10^8
Cells in layer 3	DER	1.007 ± 0.004	1.021 ± 0.004	1.00 ± 0.01
	DER_S (g_{NP}^{-1})	(2.16 ± 0.01) x10^8	(1.147 ± 0.005) x10^8	(11.29 ± 0.06) x10^8

Figure 1

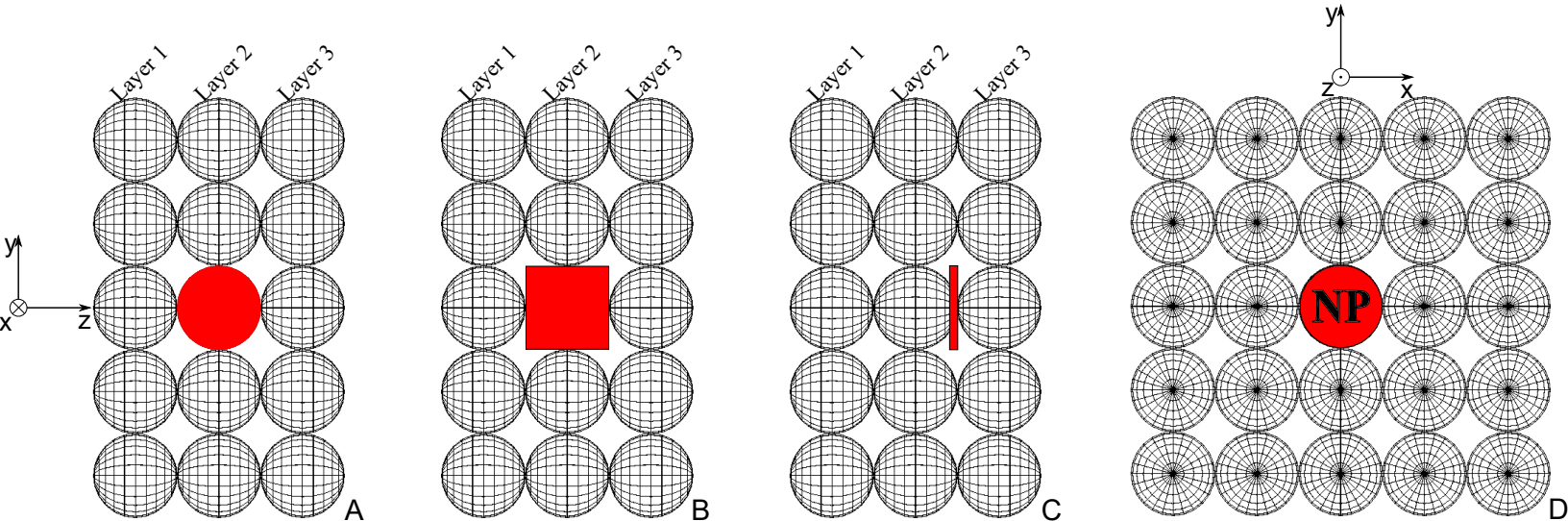
Layer 1
Layer 2
Layer 3
y
x
z
A
Layer 1
Layer 2
Layer 3
B
Layer 1
Layer 2
Layer 3
C
y
z
x
NP
D

Figure 2

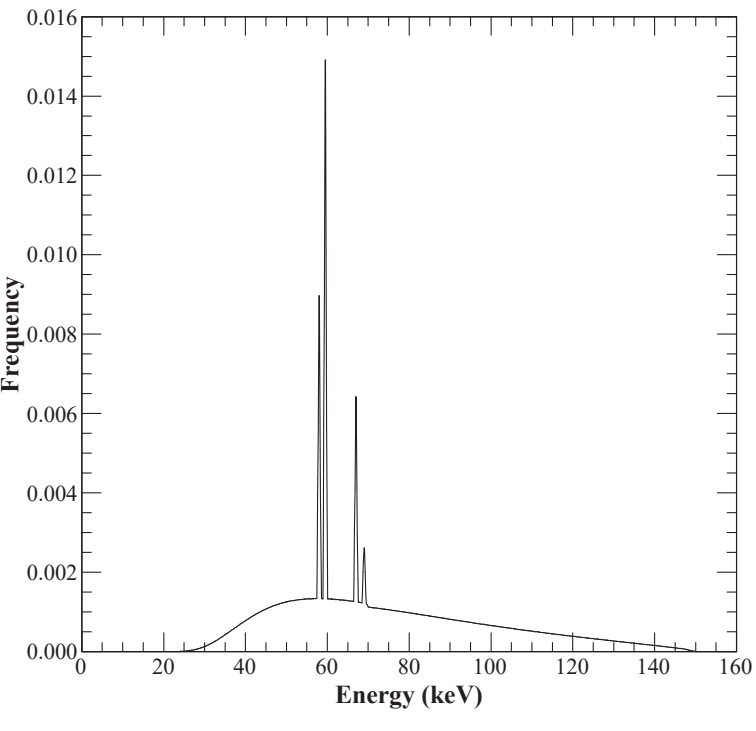
0.016
0.014
0.012
0.010
0.008
0.006
0.004
0.002
0.000
Frequency
0
20
40
60
80
100
120
140
160
Energy (keV)

A

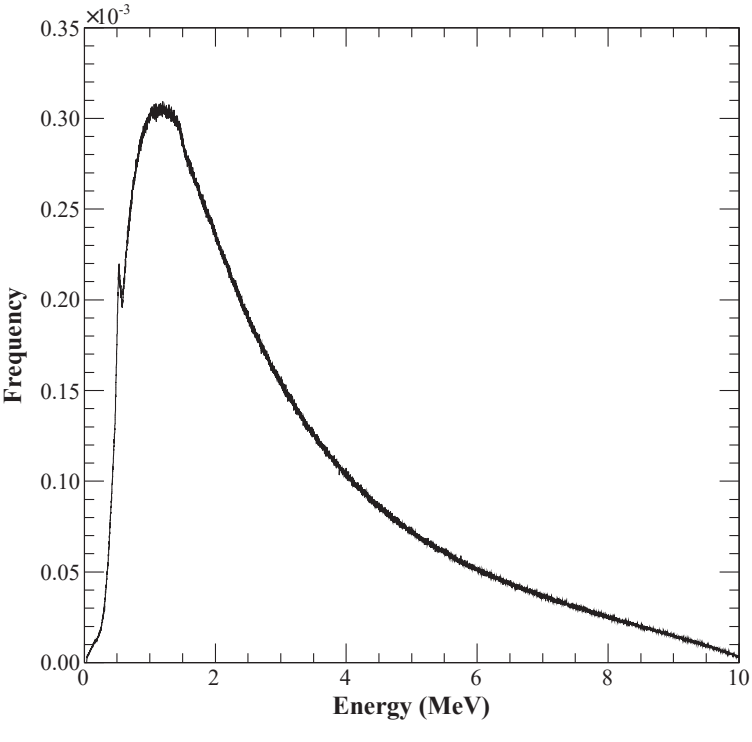
×10-3
0.35
0.30
0.25
0.20
0.15
0.10
0.05
0.00
Frequency
0
2
4
6
8
10
Energy (MeV)

B

Figure 3

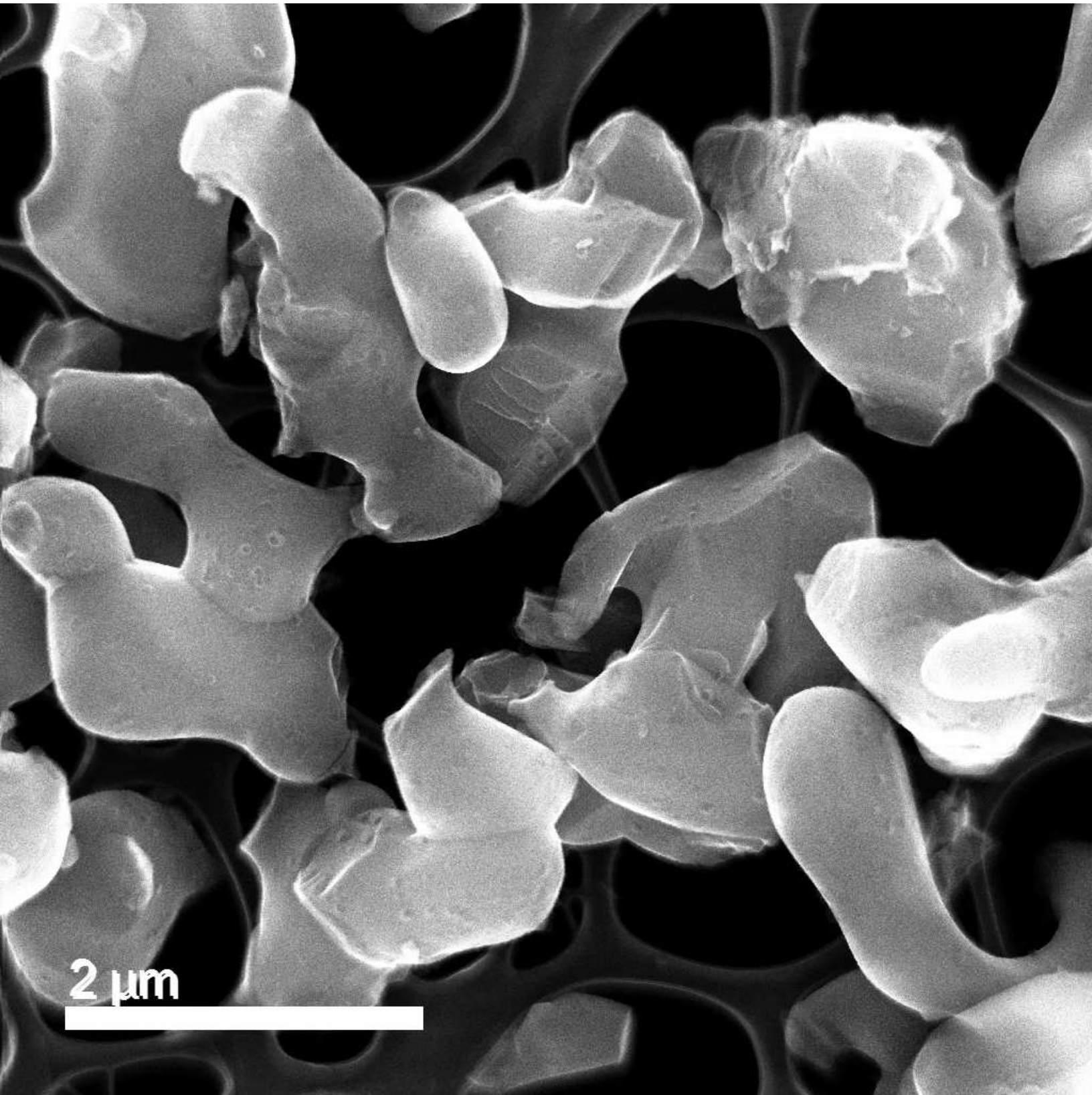

Figure 4

Click here to download high resolution image

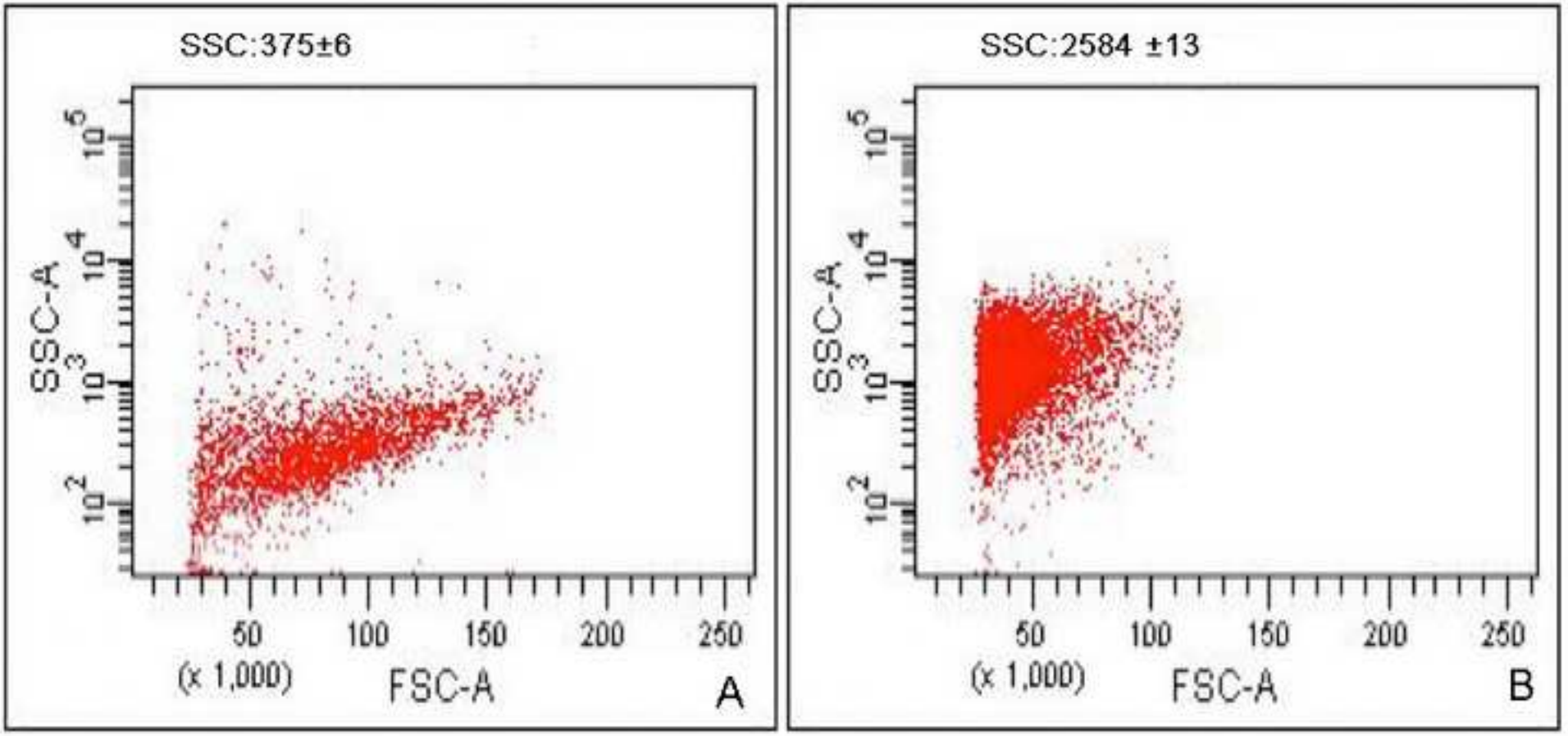

Figure 5

Click here to download high resolution image

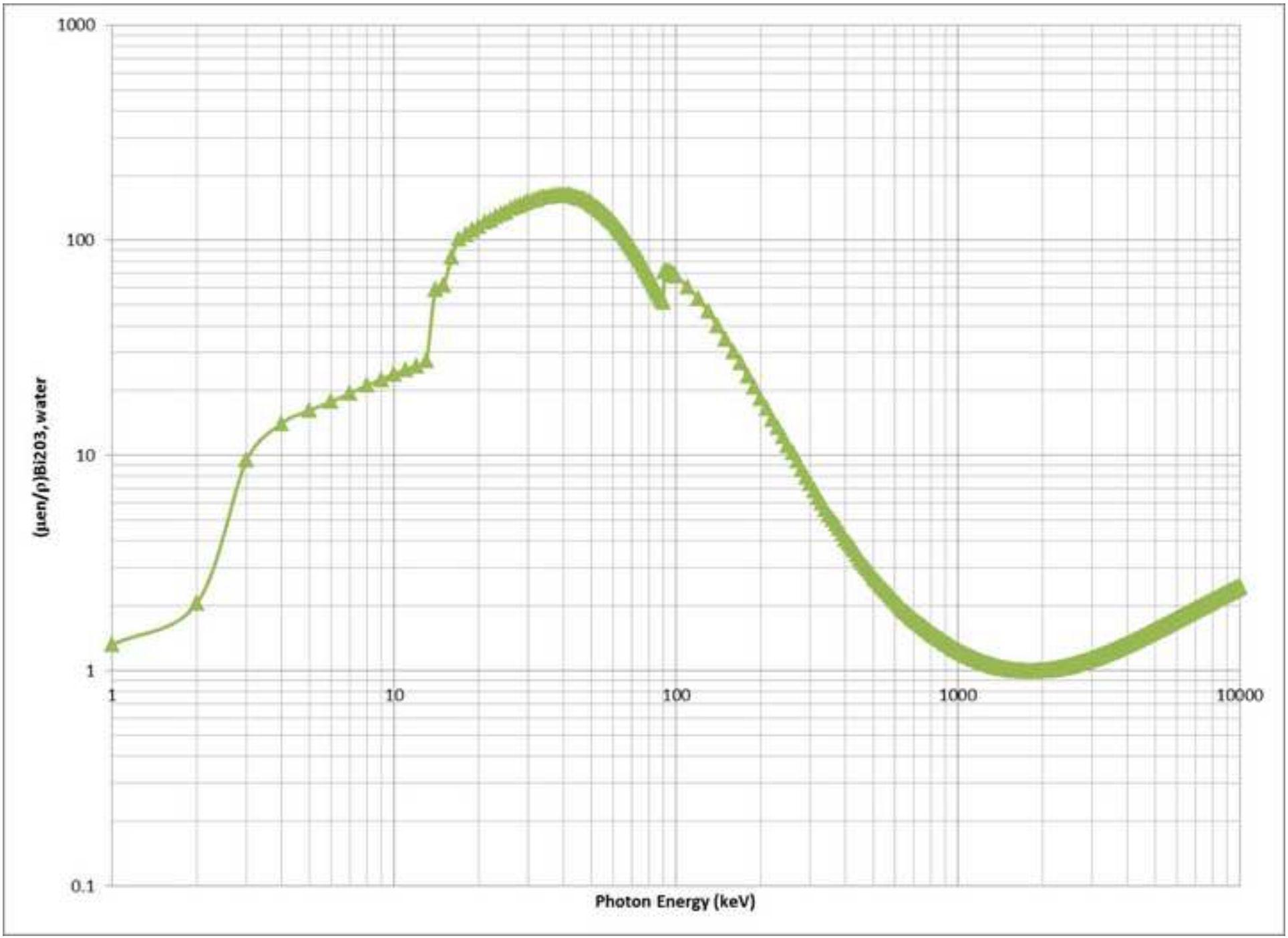

Figure 6

Click here to download high resolution image

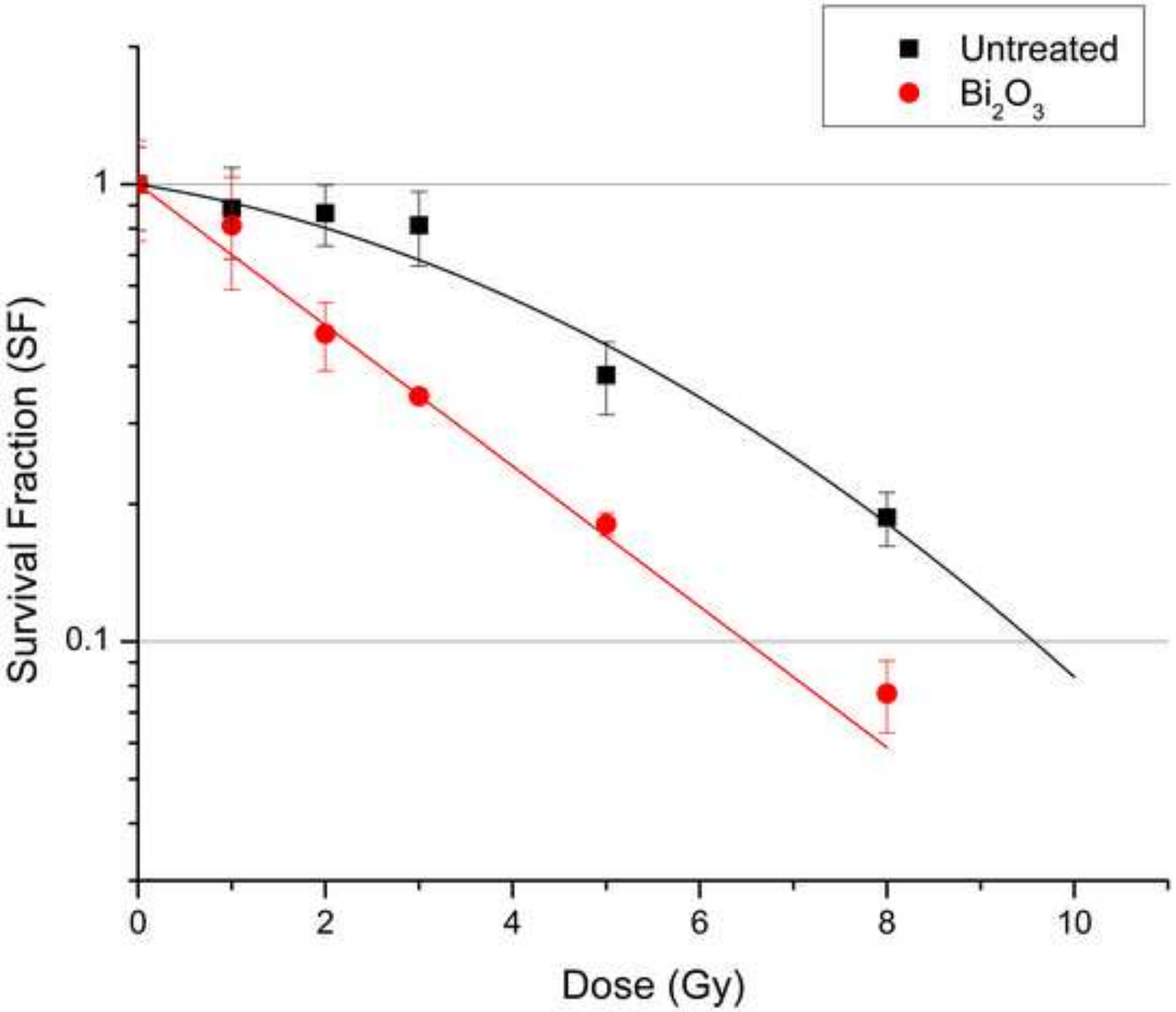

Figure 7

Click here to download high resolution image

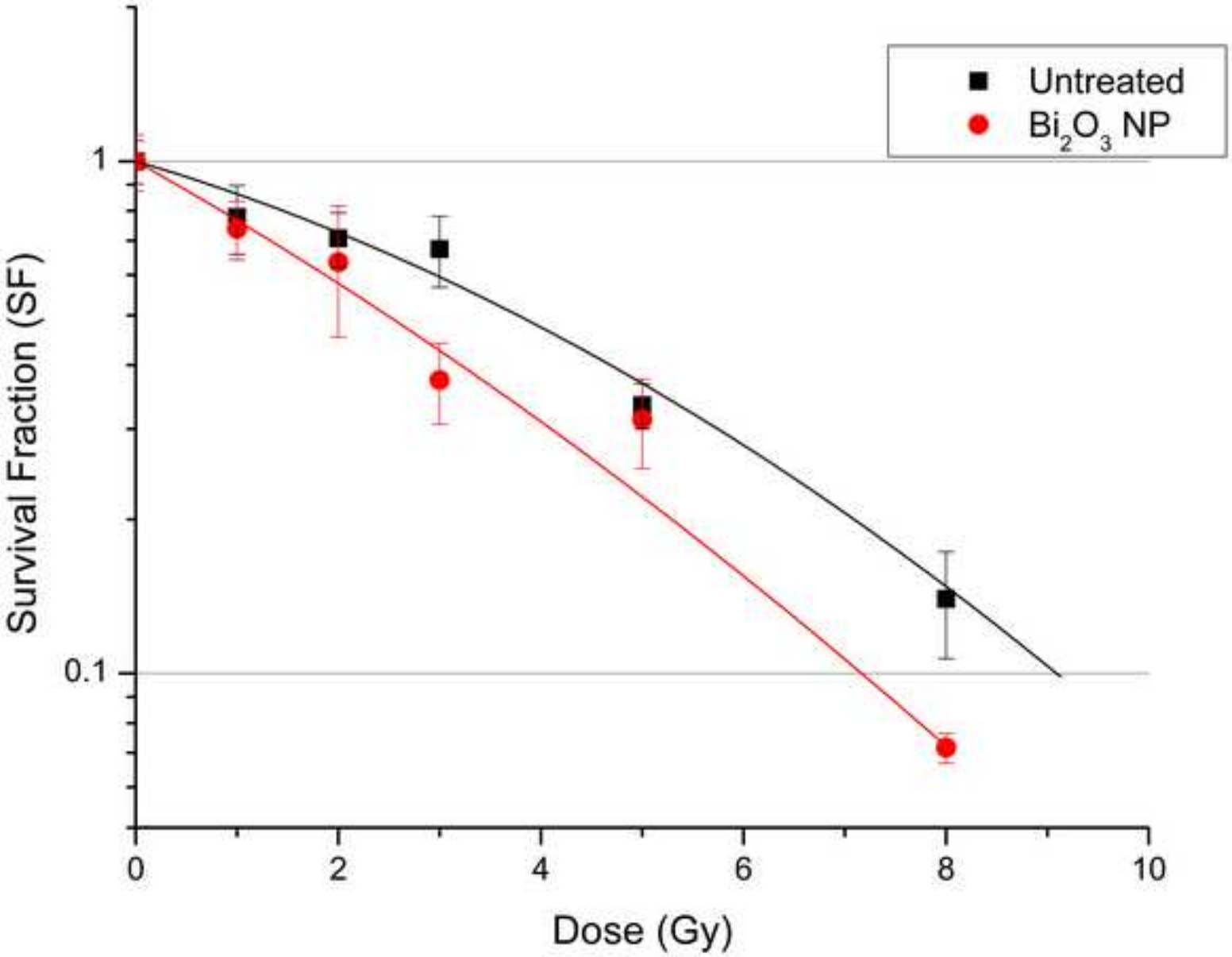

Figure 8

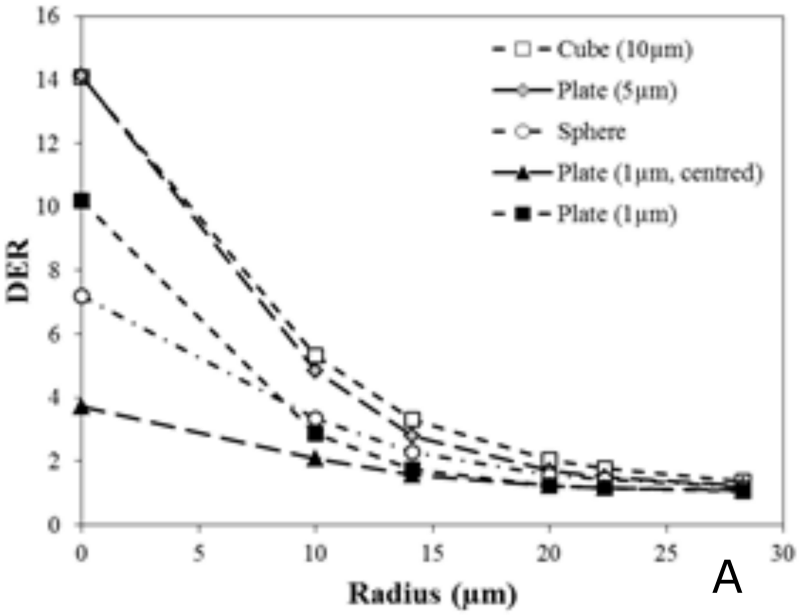
DER
Radius (µm)
Cube (10µm)
Plate (5µm)
Sphere
Plate (1µm, centred)
Plate (1µm)
A

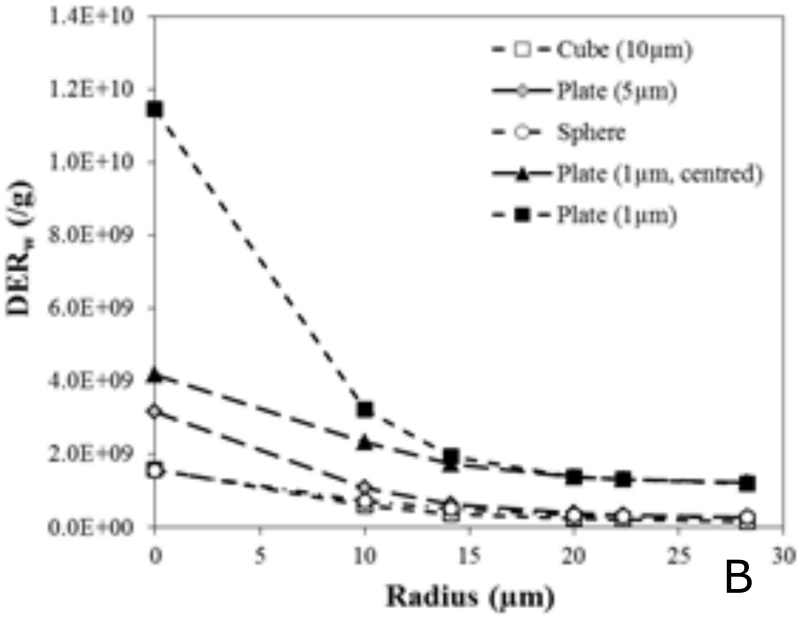
DERw (/g)
Radius (µm)
Cube (10µm)
Plate (5µm)
Sphere
Plate (1µm, centred)
Plate (1µm)
B

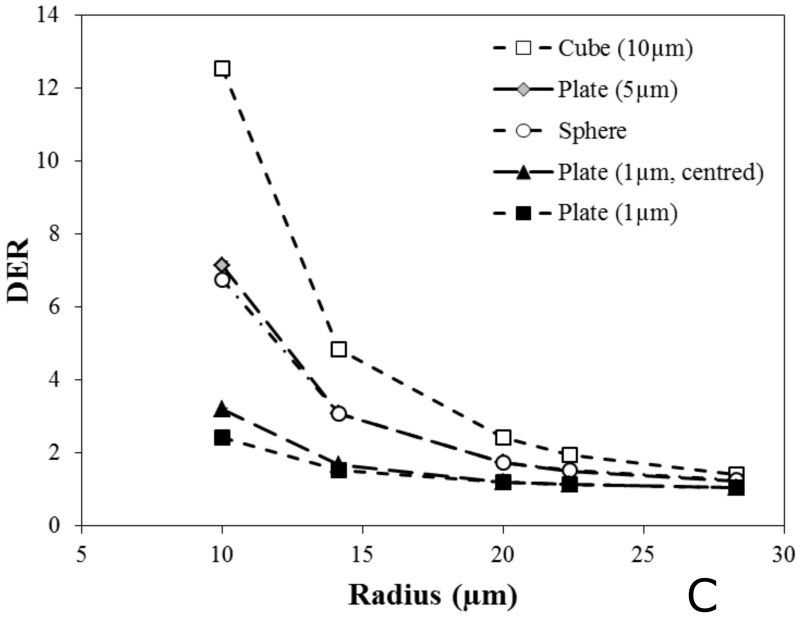
DER
Radius (µm)
Cube (10µm)
Plate (5µm)
Sphere
Plate (1µm, centred)
Plate (1µm)
C

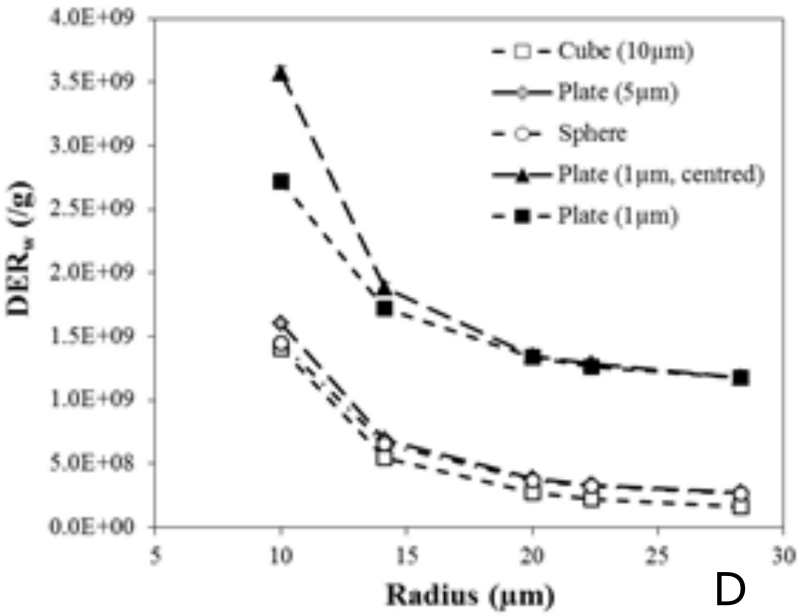
DERw (/g)
Radius (µm)
Cube (10µm)
Plate (5µm)
Sphere
Plate (1µm, centred)
Plate (1µm)
D

Figure 9

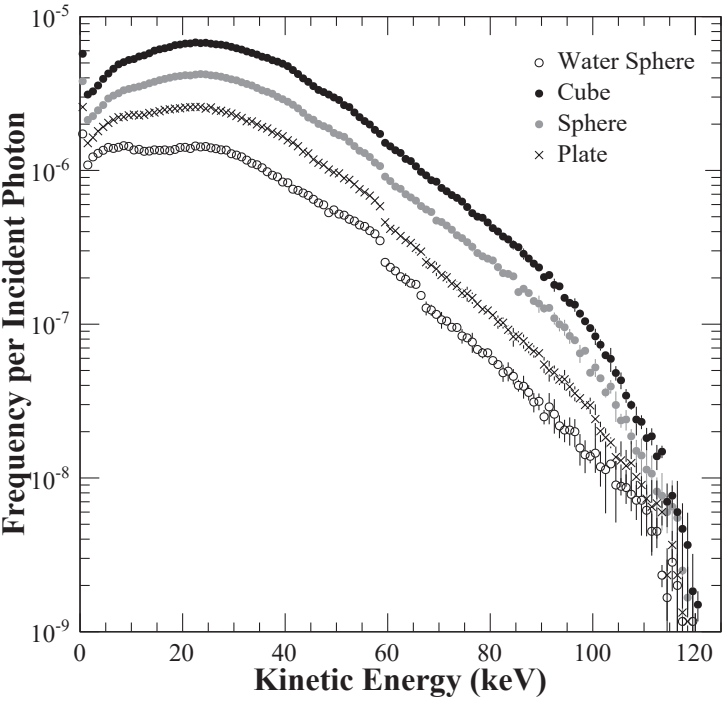

A

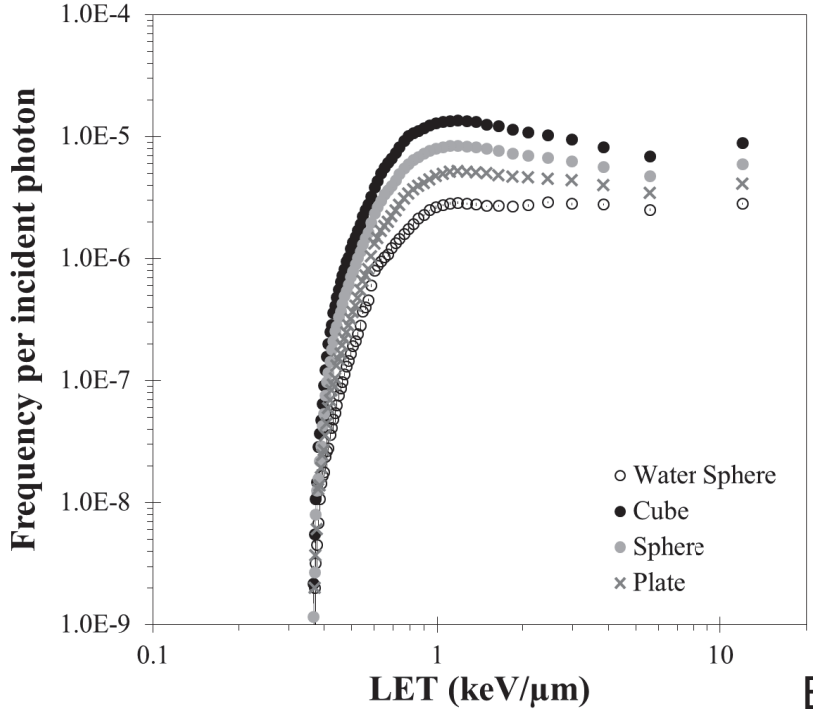

B

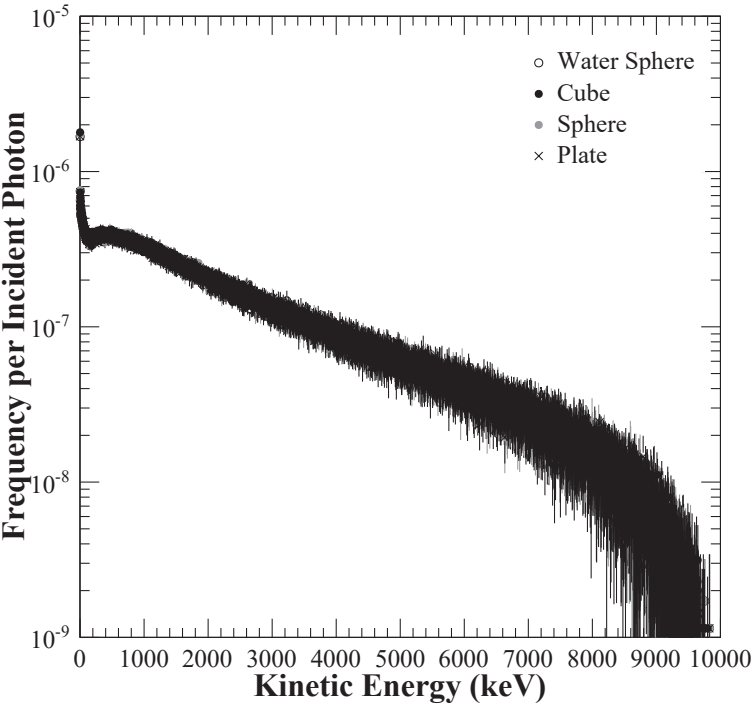

C

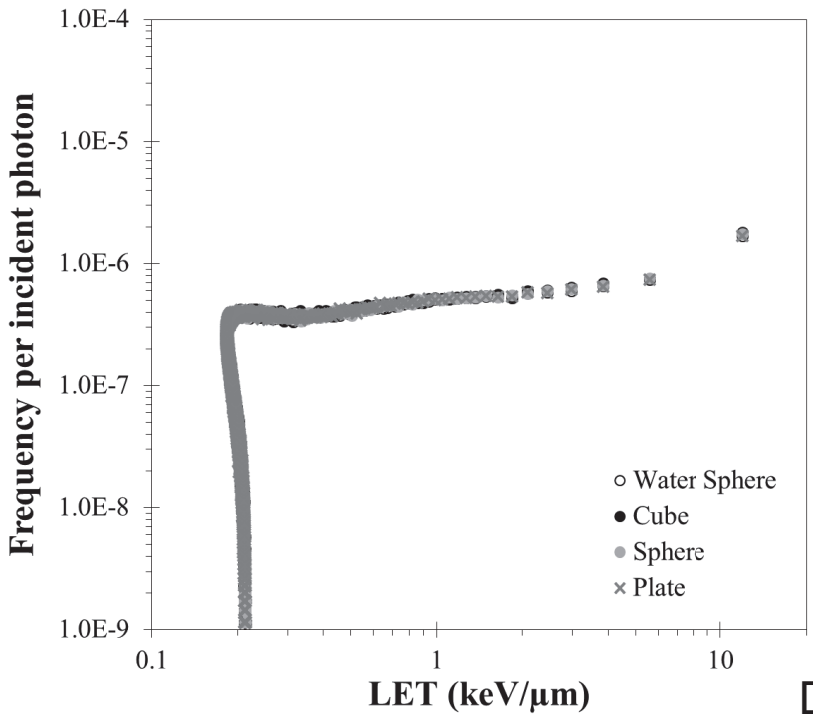

D